

Revisiting self-seeding mechanism by generating vector ultraviolet N_2^+ lasing

Jingsong Gao^{1,2,*}, Yang Wang¹, Haicheng Mei³, Jiahao Dong³, Yi Liu³, Chengyin Wu¹, Hongbing Jiang^{1,†}, Meng Han², and Yunquan Liu^{1,‡}

¹State Key Laboratory for Mesoscopic Physics and Frontier Science Center for Nano-Optoelectronic, School of Physics, Peking University, Beijing, 100871, China

²James R. Macdonald Laboratory, Department of Physics, Kansas State University, Manhattan, Kansas, 66506, USA

³Shanghai Key Lab of Modern Optical System, University of Shanghai for Science and Technology, Shanghai, 200093, China

*E-mail: jingsong@ksu.edu

†E-mail: hbjiang@pku.edu.cn

‡E-mail: yunquan.liu@pku.edu.cn

ABSTRACT

An intense femtosecond laser pulse can generate ultraviolet air lasing, offering a promising remote light source. A long-standing hypothesis is whether it is seeded by a self-generated spectral component, such as the second harmonic that is inevitably produced by the plasma gradient. Here, we report the generation of both radially and azimuthally polarized N_2^+ lasing driven by a single 800-nm cylindrical vector beam. Meanwhile, the same vector pump was applied to drive the generation of vector second harmonics in plasma. The radially polarized pump produces radially polarized second harmonics while the azimuthally polarized pump yields no second harmonic generation owing to the radial direction of plasma gradient. The absence of the azimuthally polarized second harmonic rules out the hypothesis of self-seeding by second harmonics, as both radially and azimuthally polarized N_2^+ lasing are observed with comparable intensities. By characterizing the spatial phase distribution of vector 391-nm lasing, we concluded that its phase is synchronized with the pump. These results suggest that amplified spontaneous emissions are the origin of N_2^+ lasing under the most common condition of low gas pressure, which was effectively demonstrated by theoretical simulations. Our work provides a promising method for remotely generating vector ultraviolet light sources.

Introduction

Air lasing is a phenomenon in which laser-induced air produces cavity-free coherent light¹⁻³, effectively acting as a laser. Unlike conventional lasers, which require a physical gain medium (such as a crystal, gas, or liquid) within a cavity to amplify light, air lasing occurs in the atmosphere without the need for a physical cavity. Among various types of air radiations, N_2^+ air lasing², particularly the 391-nm radiation corresponding to the transition between ground vibrational states from B to X ionic states, is one of the most debated phenomena. It has garnered significant interest due to its complex and interesting underlying mechanism⁴⁻²⁵, which results in a long-standing debate on whether there exists population inversion. Most recently, some promising applications of air lasing have been explored, such as coherent Raman spectroscopy²⁶⁻²⁹, ultraviolet supercontinuum light source³⁰⁻³², and carrier-envelope phase (CEP) tagging technology³². Previous experiments^{33,34} have clearly demonstrated that 391-nm lasing can be effectively amplified by an external seed. However, a fundamental question remains unresolved: is the 391-nm lasing process driven by one laser beam seeded by self-generated spectral components, such as self-phase modulation (SPM) or second harmonic generation (SHG)?

The prevailing use of Ti:sapphire (Ti:Sa) laser pulses complicates this question further, as the wavelength of the driving field is around 800 nm, with its second harmonic overlapping with the 391-nm transition. If the 391-nm lasing is self-seeded, it can be attributed to superfluorescence or light amplification by stimulated emission of radiation (i.e., laser action). Conversely, if the 391-nm lasing process does not involve any seeding, it is strictly amplified spontaneous emission (ASE)³⁵. For few-cycle Ti:Sa pulses as the driving field, the spectrum typically spans 550–1000 nm, and the SPM during the focusing process can easily generate a significant supercontinuum extending down to 391 nm at 1 bar pressure⁴, serving as a seed. This is reasonable because the intensity and spectral broadening of SPM are proportional to the gas pressure, sample length, and pulse peak intensity^{36,37}. Thus, for the most commonly used multi-cycle Ti:Sa pulses with durations of 35 fs as the driving field, only a very weak supercontinuum was observed near 391 nm in 1 bar *air* with a pulse energy of 6 mJ³⁸. However, within the optimal gas pressure window around 5-50 mbar that yields the strongest and clearest 391-nm lasing, SPM cannot broaden the driving field spectrum down to 391 nm because of the narrow spectral bandwidth (800 nm \pm 14 nm) and low gas pressure. To the best of our knowledge, no direct experimental observation has been reported of a supercontinuum near 391 nm at low pressures pumped by mJ-level 35-fs multi-cycle Ti:Sa lasers. Nevertheless, N_2^+ lasing at 391 nm can be easily observed from 5 to 30 mbar with a pump pulse energy

below 3 mJ^{5, 16, 18, 19, 39}, even in a dilute gas jet^{9, 40} that is too short to support the sample length needed for significant SPM. This rules out SPM as the self-seeding mechanism of 391-nm lasing in the most common case of 35-fs Ti:Sa pulse at low gas pressure.

Thus, the prevailing reliable viewpoint is that 391-nm lasing is seeded by the second harmonic generated by the charge gradient in the laser plasma filament⁴¹, which was proposed by one of the present authors⁴². In contrast to the assumption for SPM as the self-seeding at low pressure, the SHG generated by the charge gradient was indeed experimentally observed at a low pressure of 4 mbar, and it was also experimentally proved by another independent group¹⁹. However, the hypothesis of SHG self-seeding lacks direct and comprehensive evidence and relies only on observing the corresponding spectra, overlooking important spatial information of SH generated from the ponderomotive force acts. Now, we started to consider the spatial information and noticed that the Gaussian-beam-driven air lasing is always the fundamental Gaussian mode (HG₀₀ mode), while the Gaussian-beam-driven SHG from the plasma gradient should be HG₀₁ or HG₀₁ mode that contains two lobes⁴¹. It actually challenges the hypothesis of SHG self-seeding because of the mismatch of the SH mode and the air lasing mode. Therefore, investigating potential self-seeding mechanisms in 391-nm lasing remains an important and unresolved question.

Structured light with a customized profile in space and time can now be well constructed due to the development of laser tailoring techniques^{43–47}. One dramatic paradigm is cylindrical vector beams (CVBs) that possess cylindrical symmetrically polarization distribution in space⁴⁸, where the radially polarized and azimuthally polarized cases are shown in Fig. 1(a). A laser-induced plasma filament also exhibits cylindrical symmetry about the light propagation direction, resulting in a charge gradient along the radial direction in the beam cross plane, parallel to the radially polarized electric field and orthogonal to the azimuthally polarized electric field. Therefore, the key idea of our method is to introduce these features of CVBs into the laser-plasma interaction to clarify the role of the SHG in the 391-nm N₂⁺ lasing.

Here we drive the 391-nm lasing in N₂ and the second harmonic in argon with CVBs. We demonstrate the generation of both radially and azimuthally polarized 391-nm N₂⁺ lasing with similar intensities, whereas the second harmonic disappears when switching the driven field from radial to azimuthal polarization. The vector N₂⁺ lasing inherits the same CVB mode as the pump light. In contrast, the radially polarized SH belongs to a new type of radial vector beam with a higher radial order, while the azimuthally polarized pumping yields no SH signal. By analyzing the focal properties of CVBs, we show that the spatial phase of the N₂⁺ lasing is synchronized with the spatial phase of the pump light rather than being

double that of the pump light. This indicates that the phase distribution of the driving field is directly transferred to the 391-nm lasing. By combining the results of 391-nm N_2^+ lasing and the SHG in argon, we conclude that 391-nm N_2^+ lasing driven by the most commonly used mJ-level multi-cycle Ti:Sa laser pulse at optimal gas window does not involve any self-seeding mechanism and is therefore consistent with ASE.

Results

Vector ultraviolet N_2^+ lasing

The experimental setup is depicted in Fig. 1(a) (see Methods for details). An 800-nm CVB (1 kHz, 3 mJ, 35 fs) is employed as the pump light, which is focused on the 10-mbar pure nitrogen by a lens. The N_2^+ lasing is emitted from the peak density region of the laser-induced plasma. The angle of the q-plate^{49,50} is set to make the pump beam radially and azimuthally polarized, respectively, where the fast axis orientation of the q-plate and the spatial polarization distribution of the pump beam are depicted in Fig. 1(a). A linear polarizer is used to characterize the spatial polarization distribution of the N_2^+ lasing.

Figure 1(b) shows measured spectra of the 391-nm N_2^+ lasing. For the 391-nm lasing, it displays two peaks corresponding to the P and R branches of rotational transitions. The contribution from SPM can be ruled out from the weak and symmetrical pedestals on the two sides of the 391-nm lasing peak. If it is seeded by SPM extended from 800 nm, the right side of the pedestal will show some intensity above the noise level at the wavelength larger than 391 nm⁴, and will increase with wavelength. The beam intensity profiles of the generated radially and azimuthally polarized 391-nm lasing are depicted in Fig. 1(c) and Fig. 1(d), respectively. Both profiles exhibit a doughnut-shaped distribution, indicating the presence of a polarization singularity at the beam center. To examine the spatial distribution of the polarization state within the beam plane, we present the beam intensity profiles in Fig. 1(e) and Fig. 1(f) after passing through a polarizer, with the polarizer's orientation indicated above each figure. Additional polarization analyses, obtained by rotating the polarizer orientation at various positions within the beam profile, are provided in Fig. S4 of Supplementary Note 4 in Supplementary Information. The polarizations at all positions are linear, possessing radial polarization and azimuthal polarization characteristics, respectively. These results confirm that the generated radially and azimuthally polarized 391-nm lasing exhibit approximately equal intensities. Furthermore, the polarization distribution of the 391-nm lasing mirrors that of the driving field in both radial and azimuthal configurations. The laser plasma induced by CVBs features a doughnut-type cross section, similar to a fiber for generating CVBs⁵¹, which enables the generation, propagation, and

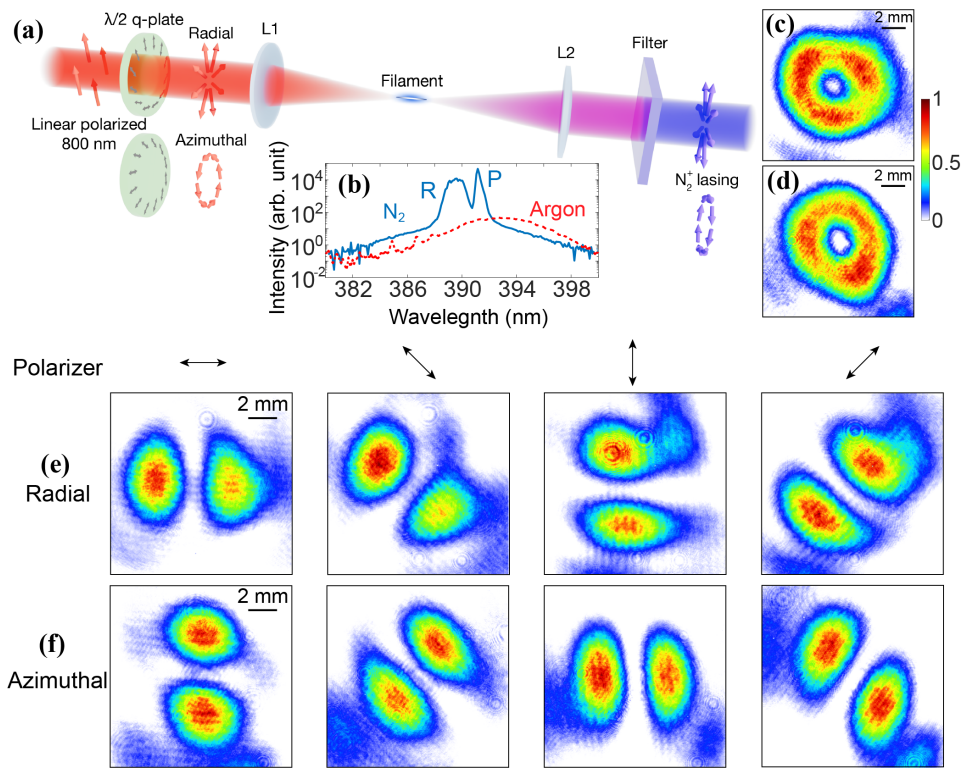


Figure 1. Generation of vector ultraviolet N_2^+ lasing. (a) Schematic of the experiment. Red and blue arrows represent electric field polarization distributions of CVB pump and vector air lasing, respectively. Grey arrows in q-plate represent fast axis locally. L1, L2 are the lenses with the focal length of 30 cm. The filter is a band-pass filter with a central wavelength of 390 and a bandwidth of 10 nm. (b) Measured 391-nm N_2^+ lasing spectrum (blue solid line) and the second harmonic spectrum from argon (red dashed line). (c, d) Measured beam profiles of the generated radially (c) and azimuthally (d) polarized 391-nm lasing. (e) Measured radially polarized 391-nm lasing beam profiles after passing a polarizer oriented along different angles marked with black arrows. (f) Corresponding experimental results for azimuthally polarized 391-nm lasing. The color bar applies to all panels c-f with the same normalized standard.

amplification of vector 391 nm N_2^+ lasing due to the cylindrically symmetric gain medium.

Second harmonics generation via plasma driven by cylindrical vector beams

The SHG can occur in an isotropic gaseous medium if the plasma within the irradiated volume is inhomogeneous. The resulting ponderomotive force acts outward from the center of the pump beam, creating an uneven electron distribution. This redistribution pushes electrons away from the center of the focused beam, ultimately leading to the SHG. The second-order polarization can be written as^{41,52},

$$\vec{P}_{2\omega} \propto \left[1/2\nabla E_P^2 + \frac{2(\vec{E}_P \cdot \nabla \ln n_e)\vec{E}_P}{\epsilon_p} \right], \quad (1)$$

where \vec{E}_P is the driving electric field in the focal plane, ϵ_p is the plasma dielectric constant, and n_e is the plasma density. In the nonuniform plasma, the last term in Eq. (1) dominates the SHG. $\nabla \ln n_e$ stands for the electron gradient along the radial direction. Therefore, the product between the driving field and the electron gradient, $\vec{E}_P \cdot \nabla \ln n_e$, will be zero for the azimuthally polarized driving field and be a maximum for the radially polarized driving field.

To eliminate the strong disturbance from N_2^+ lasing and to observe a clean beam profile of a pure SHG signal on the CCD, we select argon as the target gas in the experiment, since it exhibits no significant atomic emission lines around 400 nm. Changing gas target for comparison is reasonable because SHG beam pattern is independent of gas species, and is determined only by the charge-density gradient. Moreover, argon and N_2 have very close ionization potentials (15.76eV and 15.58eV, respectively), which leads to nearly identical charge densities under the same laser condition. The measured SH spectrum is shown in Fig. 1(b), which is close to the wavelength of N_2^+ lasing. As discussed above, the SH emission is generated at the peak of the plasma density gradient. In Fig. 2, we illustrate the theoretical and experimental results of the SH driven by CVBs in argon. Fig. 2(a) shows the calculated SH beam profile intensity with the arrows indicating the polarization state locally, driven by the radially polarized light field, based on Eq. (1). In Figs. 2(b-d), we show the corresponding beam profiles after passing a polarizer oriented along horizontal, 45° and vertical directions, respectively. The numerical results are obtained by solving wave equation, that is, Eq. (2), where the simulation details are in Methods). The theoretical result shows there are two concentric rings in the beam profile with a phase difference of π , which originates from the gradient of the doughnut-type plasma having two opposite peaks in the radial direction. This is a new type of CVBs similar to a radially polarized Bessel-Gaussian beam^{53,54}, but with only two concentric rings. It can be approximately described as the superposition of a x -polarized HG_{30} mode and a y -polarized

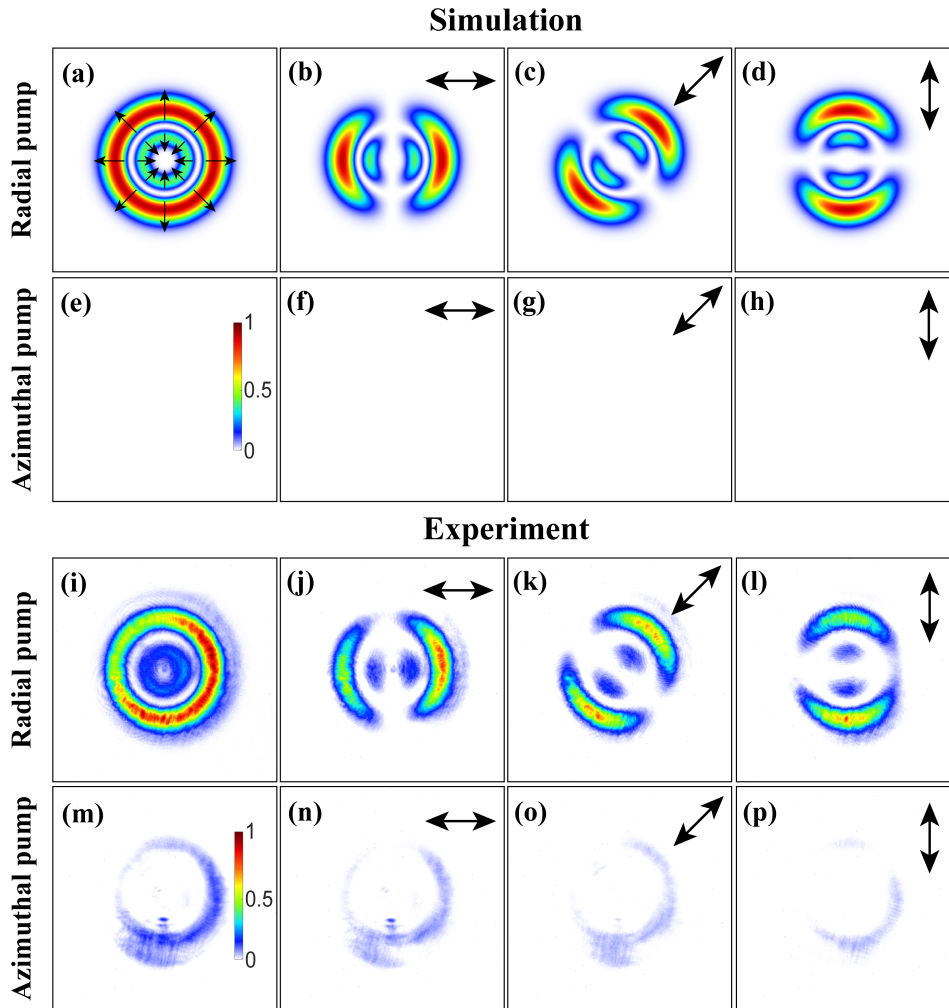


Figure 2. Second harmonic generation in argon plasma driven by cylindrical vector beams. The first column shows the beam profile of second harmonics. Columns two through four show the beam profile after passing a polarizer with the orientation marked in the upper-right corner. **(a-d)** Calculated beam intensity profile driven by radially polarized light fields. The arrows in (a) indicate the polarization state locally. **(e-h)** Calculated beam intensity profile driven by azimuthally polarized light fields. The intensity is rigorously zero in Eq. (1) for the case of azimuthal polarization. The intensities in the simulation share the color bar with the same standard in (e). **(i-l)** Measured beam intensity profile driven by radially polarized light fields. **(m-p)** Measured beam intensity profile driven by azimuthally polarized light fields. The intensities in (m-p) are normalized to those in (i-l).

HG₀₃ mode, whereas the driving field and the corresponding N₂⁺ lasing are both the superposition of a *x*-polarized HG₁₀ mode and a *y*-polarized HG₀₁ mode⁴⁸. In contrast, in the azimuthally polarized case, the gradient of the laser plasma is perpendicular to the driving electric field, i.e., $\vec{E}_p \cdot \nabla \ln n_e = 0$. Thus, the calculated SH intensity must be zero. For intuitive comparison, we also show the calculation results in Figs. 2(e-h). We have theoretically demonstrated that radially polarized driving fields can generate SH, whereas azimuthally polarized driving fields cannot generate SH at all.

We proceed to experimentally verify the calculation results. The experimental measurement results of the SHG driven by radially and azimuthally polarized light fields are shown in Figs. 2(i-l) and Figs. 2(m-p), respectively. The result in the radial case indeed shows two rings in the beam profile, matching the numerical results shown in Figs. 2(a-d), and presents a completely different CVB mode compared with the radially polarized N₂⁺ air lasing in Figs. 1(c,e). More importantly, the measured SH intensity by azimuthally polarized fields is near zero, also agreeing well with the simulation in Figs. 2(e-h). Notably, the weak signal appears in Fig. 2(m) because the cylindrical symmetry of the driving field cannot be ideal in the experiment. Even though there is a weak SH signal, its azimuthal polarization information is totally lost, as shown in Figs. 2(n-p). With excellent agreement with simulations, our experimental results convincingly proved that radially polarized driving fields can produce SHG, whereas azimuthally polarized driving fields cannot.

The absence of SHG in the azimuthal case indicates that SH plays a minimal role in the 391-nm lasing, as we have demonstrated the generation of vector N₂⁺ lasing for both radial and azimuthal polarizations with approximately equal intensities. This is reasonable and consistent with the theoretical expectation because the effective gain region is located near the peak of the driving field's intensity, where the gradient of the plasma is almost zero, i.e., there is no SHG. As a result, in the laser filamentation, the SH and the gain region are inherently not overlapped in space.

On the other hand, if SH accounts for self-seeding, the intensity of radially polarized N₂⁺ lasing in Fig. 1(c) should be expected to be significantly stronger than that of azimuthally polarized N₂⁺ lasing in Fig. 1(d), because of the existence of the radially polarized SH and the absence of the azimuthally polarized SH shown in Fig. 2. Furthermore, if N₂⁺ lasing is self-seeded by SH, the high-order pattern of radially polarized SH shown in Figs. 2(a-d,i-l) will be maintained in the amplification of the radially anisotropic gain medium¹⁸ that was induced by the permanent alignment of N₂⁺^{16,55}. This can be readily verified by the model we previously proposed¹⁸. However, the pattern of the radially polarized SH is different from that of the radially polarized N₂⁺ lasing. The mismatch between air lasing and SHG in both intensity and

spatial mode strongly rules out the self-seeding role of SHG.

Spatial phase measurement

Further experimental evidence from the perspective of spatial phase is provided in Figure 3. The key feature of the seeded air lasing is that the amplified light retains the phase of the seed^{21,22}, which can be a criterion for checking the 391-nm lasing driven by a single laser beam. In Fig. 3, we used a cylindrical lens to examine the spatial phase distribution in the beam profile. If the 391-nm lasing is phase-synchronized with the driving field, as depicted in Fig. 3(a), the two lobes after passing through a polarizer should exhibit opposite phases. Consequently, using a cylindrical lens, the two lobes cannot be focused together, and the resulting intensity pattern in the focal plane would still show two distinct stripes, as shown in Fig. 3(c). Conversely, if the 391-nm lasing is seeded by SH, the spatial phase would double. In this scenario, shown in Fig. 3(b), the two lobes after passing through a polarizer would have the same phase, allowing them to focus onto a single strip, as shown in Fig. 3(d). This would produce a dominant beam in the focal plane. Here, we intentionally assume the case of the phase doubling (actually, the SH from the plasma gradient is distinct from a normal parametric process-induced SH). In Methods, we present simulation details for the calculation of the beam focusing with the modified Richard-Wolf vectorial diffraction method for a cylindrical lens, which is described by Eqs. (3-4). Figure 3(e) illustrates our experimental results, which align with the calculated case for phase synchronization, confirming the phase relationship of the 391-nm lasing with the driving field. Notably, we only illustrate the case of the y component of the radially polarized 391 nm lasing here. Indeed, the measured phase differences of the two lobes in all panels of Figs. 1(e-f) are π .

It is worth mentioning that the N_2^+ air lasing is a non-parametric process and thereby is fundamentally different from high harmonic generation⁵⁶ and other normal parametric processes⁵⁷ in which the phase of n th harmonic is n times that of the driving field. Even in a parametric process such as SPM, any wavelength within the SPM-induced white light supercontinuum remains phase-synchronized with the driving field^{58,59}. Therefore, the fact that 391 nm is nearly twice the frequency of 800 nm does not imply that the phase of the air lasing must be twice that of the driving field.

Discussion

A supercontinuum by SPM can be characterized by B-integral³⁷, namely, $B = 2\pi/\lambda \int_0^z n_2 |E(z)|^2 dz$, where n_2 is the nonlinear refractive index linearly proportional to the gas pressure⁶⁰. It indicates that the ability of

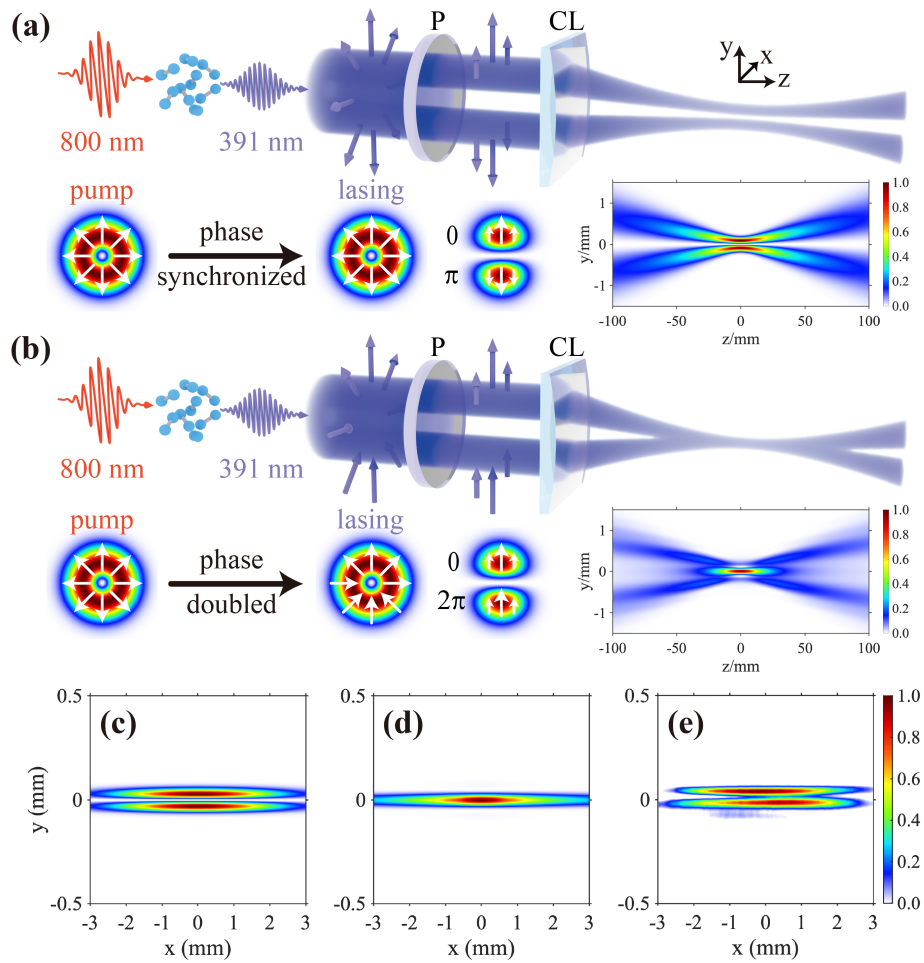


Figure 3. Phase distribution measurement of the radially polarized 391-nm N_2^+ lasing by a cylindrical lens. (a) Calculated results when the spatial phase of 391-nm lasing is synchronized with the driving field. After passing through a polarizer, the two lobes have a phase difference of π . Blue and white arrows represent local polarization direction of air lasing. P is polarizer, CL is cylindrical lens. (b) Calculated results when the spatial phase of 391-nm lasing is double that of the driving field. After passing through a polarizer, the two lobes have a phase difference of 2π . Blue and white arrows represent local polarization direction of air lasing. P is polarizer, CL is cylindrical lens. (c, d) Calculated beam profiles in the focus plane in the scenarios of (a) and (b), respectively. (e) Experimental result.

spectral broadening is generally proportional to the gas pressure, propagation distance, and peak intensity of light (pulse energy over pulse duration)³⁶. In previous experiments, the SPM extending spectrum from 800 nm to 391 nm was experimentally observed only in air at 1 bar; it is relatively strong with a broadband few-cycle pump⁴ but very weak with a conventional multi-cycle pump with pulse energies of 6 mJ³⁸ and 8 mJ⁶¹, whose pulse energies are relatively high. Nevertheless, for most common cases of N₂⁺ air lasing studies, 391-nm lasing was driven by a multi-cycle 35-fs Ti:Sa laser under the condition of an optimal gas pressure window below 100 mbar⁴², where 391-nm lasing can be easily observed from 5 to 30 mbar with a pump pulse energy below 3 mJ^{5, 16, 18, 19, 39}. Moreover, pulse energy and gas pressure can even reach 1.1 mJ and 5 mbar⁶², and propagation distance can tolerate the length of a dilute gas jet^{9, 40}. Obviously, the B-integrals in these common cases can be about 2 or 3 orders of magnitude smaller than that of the 1-bar case. However, just a twofold decrease in the B-integral, below an order-of-magnitude reduction, can markedly suppress spectral broadening⁶³. Consequently, there is no previous experimental evidence reported that a multi-cycle 35-fs Ti:Sa laser can extend its narrow-band spectrum from 800 nm to 400 nm under low pressure. In our experiment, even a side fluorescence signal can be easily detected over a small solid angle¹⁶, whereas the supercontinuum with high collimation was never observed around 400 nm despite capturing the whole forward emission cone. Even in our recent experiment employing 3.7-fs single-cycle pulses as the driving field, it remains difficult to extend the super-broad spectrum of the driving field down to 400 nm at low pressure³¹. Therefore, SPM should not be treated as the self-seeding for the most common case driven by multi-cycle laser pulses at low gas pressure. Citing the white light from SPM obtained at 1-bar gas pressure as evidence of the self-seeding mechanism for the most common low-pressure case is not appropriate.

On the other hand, as shown in Figs. 1 and 2, we can generate both radially and azimuthally polarized air lasing with comparable intensities; however, because of a well-understood physical mechanism, SHG from the plasma gradient occurs only for the radial case, not for the azimuthal case. As we discussed above, due to the existence of air lasing and the absence of SH in azimuthally polarized pumping, it is solid evidence that SH contributes a minimal part to the 391-nm lasing. Therefore, after ruling out the SPM and SHG as the self-seeding, we believe the 391-nm lasing originates from the ASE process. Now, we will discuss how ASE becomes a vector beam in N₂⁺ lasing.

It is generally accepted that the wavefronts of ASE from different individual emitters are incoherent with each other. Although the phase of each wavefront is uniform, the ensemble of all emitters manifests as unpolarized fluorescence. However, previous studies point out that the spatial coherence of ASE is

determined by gain geometry^{64–66}. With a specific anisotropic gain medium, spontaneous emissions could be amplified into a highly linearly polarized beam⁶⁷, an optical vortex⁶⁸, a CVB⁶⁹, and a spatially coherent light source via Dicke superradiance and subradiance⁷⁰. In our previous study¹⁶, based on the MO-ADK theory^{71,72}, we have demonstrated—both experimentally and theoretically—that preferential ionization of N_2 induces a permanent alignment of N_2^+ . This permanent alignment leads to an anisotropic gain with a maximum amplification direction along the pump light’s polarization, which is independently proved by another theoretical work with the perspective of the anisotropic quantum coherence⁵⁵. Thus, if the pump light is a CVB, the gain will exhibit cylindrical symmetry, the theoretical model of which was built in our previous study¹⁸. By the way, previous studies have demonstrated that transient alignment can modulate air lasing intensity under a pump-probe scheme^{73,74}. This is because, combining permanent alignment, the averaged alignment degree changes with time delay. However, the existence of permanent alignment makes the time-averaged alignment degree always greater than 1/3, making air lasing polarization align with that of the pump light. Here, due to the absence of the seed (single pump), we only employed the theoretical model for the simulations about how ASE becomes a vector beam, where the effect of transient alignment is ignored. The details of the model and simulations are in Methods, which is described by Eqs. (5-6).

In Fig. 4, we show simulations of ASE processes in the radially anisotropic gain when the driving electric field is a radially polarized beam. Following the principle of ASE, the seed is a random spontaneous-emission source including some random noise light spots, where each light spot has a random amplitude, a random phase, a random polarization, and a random location, as shown in the first column of Fig. 4. The energies of these seeds are photon-level. Figs. 4(a-d) show the amplification and propagation processes of ASE wavefronts originating from four individual emitters of random spontaneous emissions, respectively. The amplification factors from photon level in the first column to nanojoule in the fifth column are about 10^{10} times. As the simulations demonstrate, regardless of the initial distribution of spontaneous-emission noise, the output ASE wavefront is always radially polarized. This is because, as Eqs. (5-6) present, E_x and E_y are coupled with each other in CVB-induced cylindrically symmetric gain by the macroscopic polarization of N_2^+ medium. As a result, even though the individual light spots in the initial spontaneous-emission seed are mutually incoherent, the competition during amplification and propagation through the gain medium synchronizes spatial phase, yielding a coherent, radially polarized ASE wavefront. Here, we show only four cases; in fact, we performed many independent runs starting with different random spontaneous emissions, and in every case the ASE ultimately evolved to be radially

polarized. Therefore, the ensemble of all ASE wavefronts collectively manifests as a radially polarized beam, the same as experimental results presented in Figs. 1(c,e).

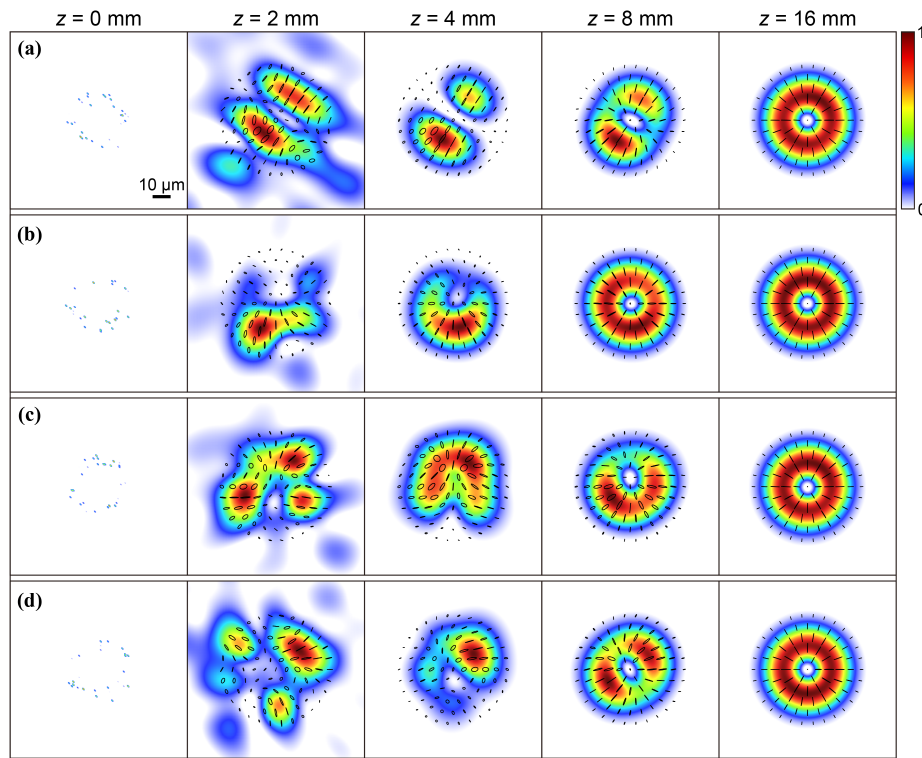


Figure 4. Simulated amplified spontaneous emissions in a radially anisotropic gain medium. (a-d) Beam profiles of ASE at different propagation distances in the radial gain, each amplified from an independent random spontaneous-emission source shown in the first column. Each spontaneous-emission source has some random noise light spots with random amplitudes, random phases, and random locations. Columns two through five correspond to propagation distances of 2 mm, 4 mm, 8 mm, and 16 mm, respectively. Black ellipses and lines represent directions and states of polarization locally. A shared color bar is used for all panels.

In Fig. 5, we show simulations of ASE processes in the azimuthally anisotropic gain when the driving electric field is an azimuthally polarized beam. Similarly, regardless of the initial distribution of spontaneous emission noise, every output ASE wavefront consistently evolved into an azimuthally polarized state, collectively manifesting as an azimuthally polarized beam. This is consistent with the experimental result shown in Figs. 1(d,f). In addition, when the driving electric field is an arbitrary CVB between radial and azimuthal polarization states, all of the ASE wavefronts will exhibit the same vectorial mode as the driving field. Furthermore, when the driving electric field is linearly polarized,

the ASE wavefronts will be linearly polarized with the same polarization direction as the driving field. Conversely, when there is no permanent alignment of N_2^+ , i.e., $\langle \cos^2 \theta \rangle$ equals to $\langle \sin^2 \theta \rangle$ in the theoretical model, the gain medium will be isotropic. As the corresponding simulations presented in Fig. S3 in Supplementary Note 3 of Supplementary Information, the individual output ASE wavefronts amplified in the isotropic gain medium exhibit random polarization states and thereby are incoherent with each other, collectively manifesting as unpolarized fluorescence. This is consistent with normal cases of ASE^{64–66,75,76}.

Generally, in a gain medium with a fixed cross-section and a fixed gain coefficient, the intensities of forward and backward ASEs are comparable. However, the laser filament is tapered¹⁹, consisting of a long narrow-to-broad section followed by a short broad-to-narrow section. In such a narrow-to-broad geometry, the backward ASE experiences a gradually decreasing gain cross-section along the propagation direction, which makes it more prone to diffract out of the gain region than the forward case. Previous study demonstrated that forward emissions are more than three orders of magnitude stronger than backward emissions in this tapered gain medium⁷⁷. More importantly, the gain lifetime with significant amplification in N_2^+ lasing is about 10-20 ps^{73,78,79}, which corresponds to 3-6 mm optical path. This makes the gain coefficient fundamentally different in the forward emission and backward emission: the forward emission experiences a fixed gain coefficient because the time between ions excited by the pump light and stimulated by the forward emission is fixed; in contrast, the backward emission experiences a continuously decreasing gain coefficient because the time delay between exciting and stimulating of ions increases with propagating, resulting in almost no optical amplification at the second half of the backward propagation in laser plasma. These two aspects make backward ASE hard to be detected in the experiment.

To be summarized, as previous studies present^{67–69}, not all cases of ASE manifest as unpolarized fluorescence. In our case, we demonstrated that, owing to the permanent alignment of N_2^+ , the amplification of randomly spontaneous-emission seeds at 391 nm into CVBs is an inevitable outcome in such a cylindrically symmetric anisotropic gain medium.

Conclusions

In conclusion, our study provides critical insights into the generation mechanism of N_2^+ lasing at 391 nm and the ponderomotive force acts in plasma, specifically addressing the role of self-seeding by the second harmonic. We generated both radially and azimuthally polarized 391-nm lasing driven by a single pump beam. By analyzing the spatial phase distribution, we demonstrated that the lasing phase is

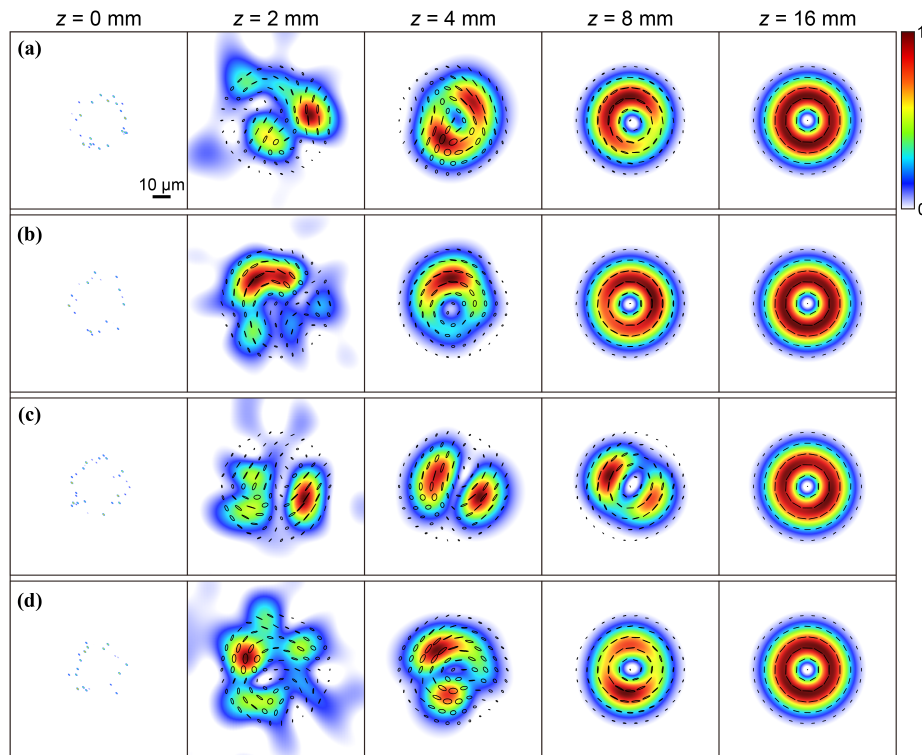


Figure 5. Simulated amplified spontaneous emissions in an azimuthally anisotropic gain medium.

(a-d) Beam profiles of ASE at different propagation distances in the azimuthal gain, each amplified from an independent random spontaneous-emission source shown in the first column. Each spontaneous-emission source has some random noise light spots with random amplitudes, random phases, and random locations. Columns two through five correspond to propagation distances of 2 mm, 4 mm, 8 mm, and 16 mm, respectively. Black ellipses and lines represent directions and states of polarization locally. A shared color bar is used for all panels.

synchronized with the driving field. Because azimuthally polarized pumping yields no SH signal yet still produces azimuthally polarized air lasing with an intensity comparable to that of the radially polarized case, second harmonic self-seeding is effectively ruled out. Otherwise, the intensity of radially polarized air lasing should be expected to be significantly stronger than that of the azimuthally polarized one. Our experimental results suggest the 391-nm lasing originates from the ASE process under the most common condition of low pressure and 800-nm multi-cycle pulse pumping. It should be mentioned that, compared with ASE, SPM can be a significant self seed under the condition of relatively high pulse energy at 1-bar gas pressure or few-cycle pulse pumping, owing to the related strong spectral broadening ability. We then performed simulations to explain how ASE evolves into a CVB with a theoretical model of cylindrically symmetric gain medium that is derived from the experimentally confirmed permanent alignment of N_2^+ . We also demonstrated the implementation of a special high-order radially polarized SH from the gradient of the laser plasma. This work not only resolves a key aspect of the lasing mechanism but also introduces a method for remotely generating ultraviolet vectorially structured light fields, offering new possibilities for applications in advanced remote sensing and laser physics.

Methods

Experimental Setup

The s-polarized Gaussian laser pulses are launched from a Ti:Sa amplifier (Spectra-Physics Spitfire Ace) with a central wavelength of 800 nm, a pulse duration of 35 fs, a repetition of 1 kHz, and a single pulse energy of 3 mJ. After passing through a thin half-wave q-plate, the 800 nm Gaussian beam becomes a CVB with spatially variant polarization. Note that the q-plate was selected intentionally to avoid generating SH by itself. Then, the CVB is focused on the 10-mbar pure nitrogen or argon gas by a lens with a focal length of 30 cm. The corresponding peak intensity at the focus is estimated to be the order of 10^{14} W/cm² regarding defocusing effect and relatively low peak intensities of CVBs. In nitrogen, the N_2^+ lasing is emitted from the peak density region of the laser-induced plasma. A 650-nm short-pass filter was used to move out the driving field. Then, we directly measure the spectrum by a fiber head connected to a grating spectrometer. In order to capture a pure beam profile of N_2^+ lasing, a band-pass filter with a central wavelength of 390 nm and a bandwidth of 10 nm was used to move out other spectral components. After the band-pass filter, the beam profile was recorded by a CCD. In argon, the SH emission, generated at the peak of the plasma density gradient, is recorded by the CCD and the spectrometer after the 650-nm

shortpass filter. The angle of the q-plate is set to make the pump beam radially and azimuthally polarized, respectively, where the fast axis orientation of the q-plate and the spatial polarization distribution of the pump beam are depicted in Fig. 1(a). A linear polarizer is used to characterize the spatial polarization distribution of the N_2^+ lasing and the SH. A cylindrical lens with a focal length of 1 m is used to measure the spatial phase of vector air lasing.

Numerical Simulations

Second harmonic generation simulations. The polarization for second harmonic generation (SHG) from the ponderomotive force in plasma is given by Eq. (1). In laser-induced plasma, the second term on the right side dominates the SHG. This is because the first term is a purely irrotational polarization without curl, giving rise to some longitudinal mode and thereby no radiation at far field⁵². Thus, we neglect the first term and substitute Eq. (1) in the wave equation under the condition of a slowly varying approximation, namely,

$$\frac{\partial^2 \vec{E}_{SH}}{\partial x^2} + \frac{\partial^2 \vec{E}_{SH}}{\partial y^2} + 2ik \frac{\partial \vec{E}_{SH}}{\partial z} = -\frac{2\mu\omega^2\chi^{(2)}}{\epsilon_p} (\vec{E}_P \cdot \nabla \ln n_e) \vec{E}_P, \quad (2)$$

where \vec{E}_{SH} is the electric field of SHG, k is the wavenumber of the driving electric field, ω is the angular frequency of the driving electric field, and μ is the permeability. The equations are solved using the split-step Fourier method. In the calculation for the driving electric field of a CVB, we neglected the z -direction dependence of the plasma density because we only considered the spatial transverse distribution of the electric field of the SHG (see Supplementary Note 1 of Supplementary Information for numerical details).

Focusing simulations. We applied the principle of Richard-Wolf vectorial diffraction method⁸⁰ to simulate the focusing process of a CVB. In the experiment, we used a cylindrical lens instead of a spherical lens to focus the vector air lasing. A cylindrical lens focuses the light in only one dimension (x or y direction), allowing us to observe two clear and distinct stripes rather than two barely noticeable and tiny spots. In order to make the simulation consistent with the experimental setup, we modified the Richard-Wolf method so that it can be applied to a cylindrical lens (See supplementary Note 2 of Supplementary Information). Thus, the electrical field after a cylindrical lens without the approximation near the focus is given by,

$$\vec{E}(x, y, z) = -\frac{ik}{2\pi} \int_{-\theta'_m}^{\theta'_m} \int_{-\frac{D}{2}}^{\frac{D}{2}} P(\theta') E(x', y') \vec{u} \frac{e^{ikR}}{R} K(\chi) dS, \quad (3)$$

where $\vec{E}(x, y, z)$ is the electric field after a cylindrical lens, (x, y, z) is the corresponding Cartesian coordinate system, k is the wavenumber, (x', y', z') is the Cartesian coordinate system with the center of the lens

as the origin before focusing, θ' is the polar angle in the output pupil of the focusing system given by $y' = f \sin \theta'$, θ'_m is the maximum angle determined by the numerical aperture of the lens ($\frac{D}{2} = f \sin \theta'_m$, f is the focal length, D is the diameter of the aperture), $P(\theta') = \sqrt{\cos \theta'}$ is the pupil apodization function, $E(x', y')$ is the amplitude of incident electric field before the lens in the pupil plane, z' is parallel to z , $K(\chi) = \cos \chi$ is the inclination factor, and χ is the angle between \vec{R} and \vec{s} . As shown in Fig. S2 in Supplementary Note 2 of Supplementary Information, \vec{s} is the unit vector of propagation direction of the ray after the lens, \vec{r} is the position vector with the focus as the origin, and \vec{R} indicates the displacement from the pupil plane to the image plane. Noticing that $P(\theta)E(x', y')\vec{u}$ represents the electrical field after the lens in the pupil plane, where \vec{u} is given by

$$\vec{u} = \cos \phi \begin{pmatrix} \frac{x'}{\sqrt{x'^2 + y'^2}} \vec{e}_x \\ \frac{y'}{\sqrt{x'^2 + y'^2}} \cos \theta' \vec{e}_y \\ \frac{y'}{\sqrt{x'^2 + y'^2}} \sin \theta' \vec{e}_z \end{pmatrix} + \sin \phi \begin{pmatrix} -\frac{y'}{\sqrt{x'^2 + y'^2}} \vec{e}_x \\ \frac{x'}{\sqrt{x'^2 + y'^2}} \cos \theta' \vec{e}_y \\ \frac{x'}{\sqrt{x'^2 + y'^2}} \sin \theta' \vec{e}_z \end{pmatrix}, \quad (4)$$

where ϕ is a factor determining the percent of radial and azimuthal amplitude, \vec{e}_x , \vec{e}_y , and \vec{e}_z are the unit vectors of x, y, and z directions, respectively. It should be noted that $\phi = 0^\circ$ represents radial polarization and $\phi = 90^\circ$ represents azimuthal polarization. In the case of a cylindrical lens, variables follow the relationships that are $\vec{s} = -\sin \theta' \vec{e}_y + \cos \theta' \vec{e}_z$, $\vec{r} = x\vec{e}_x + y\vec{e}_y + z\vec{e}_z$, $\vec{x}' = x'\vec{e}_x$, $\vec{R} = f\vec{s} - \vec{x}' + \vec{r}$, and $dS = dx'dy' = f dx' d\theta'$. Combining Eq. (3) and Eq. (4), we can simulate x, y and z component of electric field distribution at any distance in focusing process (See supplementary Note 2 of Supplementary Information for numerical details).

Amplified spontaneous emission simulations. In our previous study¹⁶, based on the MO-ADK theory^{71,72}, we have demonstrated that preferential ionization of N_2 induces a permanent alignment of N_2^+ . We show that the permanent alignment leads to an anisotropic gain with a maximum amplification direction along the pump light's polarization, which is also proved by another theoretical work with the perspective of the anisotropic quantum coherence⁵⁵. As a result, when the pump light is a cylindrical vector beam, the corresponding anisotropic gain medium will exhibit cylindrical symmetry. We derived the theory model of this cylindrically anisotropic gain medium in our previous work, where the corresponding macroscopic polarization is given by¹⁸

$$P_x = C[\langle \cos^2 \theta \rangle (E_x \cos^2 \phi + E_y \sin \phi \cos \phi) + \langle \sin^2 \theta \rangle (E_x \sin^2 \phi - E_y \sin \phi \cos \phi)], \quad (5)$$

and

$$P_y = C[\langle \cos^2 \theta \rangle (E_x \sin \varphi \cos \varphi + E_y \sin^2 \varphi) - \langle \sin^2 \theta \rangle (E_x \sin \varphi \cos \varphi - E_y \cos^2 \varphi)], \quad (6)$$

where P_x and P_y are the x and y components of the macroscopic polarization, respectively, C is a constant, φ is the azimuthal angle in xy plane, E_x and E_y are the x and y components of the electric field of 391 nm lasing, respectively, $\langle \cos^2 \theta \rangle$ and $\langle \sin^2 \theta \rangle$ are the permanent alignment degrees of N_2^+ that are parallel to the radial and azimuthal directions, respectively. As we can see, in the case of a cylindrical vector pump beam, the macroscopic polarization is a function of both the x and y components of the seed electric field, namely, E_x and E_y are coupled with each other in such a gain medium. Substituting Eq. (5) and Eq. (6) into wave equation, we can simulate how ASE evolve into a CVB during process of propagation and amplification, as shown in Fig. 4 and Fig. 5 (see Supplementary Note 3 of Supplementary Information for numerical details).

Data availability

The data that support the findings of this study are available from the corresponding author on request.

Code availability

The code that supports the findings of this study is available from the corresponding author on request.

References

1. Dogariu, A., Michael, J. B., Scully, M. O. & Miles, R. B. High-gain backward lasing in air. *Science* **331**, 442–445 (2011).
2. Yao, J. *et al.* High-brightness switchable multiwavelength remote laser in air. *Phys. Rev. A* **84**, 051802 (2011).
3. Nie, Z. *et al.* Bidirectional cascaded superfluorescent lasing in air enabled by resonant third harmonic photon exchange from nitrogen to argon. *Phys. Rev. Lett.* **133**, 063201 (2024).
4. Xu, H., Lötstedt, E., Iwasaki, A. & Yamanouchi, K. Sub-10-fs population inversion in N_2^+ in air lasing through multiple state coupling. *Nat. Commun.* **6**, 8347 (2015).
5. Liu, Y. *et al.* Recollision-induced superradiance of ionized nitrogen molecules. *Phys. Rev. Lett.* **115**, 133203 (2015).

6. Zhang, Q. *et al.* Sub-cycle coherent control of ionic dynamics via transient ionization injection. *Commun. Phys.* **3**, 50 (2020).
7. Yao, J. *et al.* Population redistribution among multiple electronic states of molecular nitrogen ions in strong laser fields. *Phys. Rev. Lett.* **116**, 143007 (2016).
8. Azarm, A., Corkum, P. & Polynkin, P. Optical gain in rotationally excited nitrogen molecular ions. *Phys. Rev. A* **96**, 051401 (2017).
9. Britton, M. *et al.* Testing the role of recollision in n 2+ air lasing. *Phys. Rev. Lett.* **120**, 133208 (2018).
10. Ando, T. *et al.* Rotational, vibrational, and electronic modulations in N₂⁺ lasing at 391 nm: Evidence of coherent B²Σ_u⁺—X²Σ_g⁺—A²Π_u coupling. *Phys. Rev. Lett.* **123**, 203201 (2019).
11. Zhang, X. *et al.* Coherent control of the multiple wavelength lasing of N₂⁺: coherence transfer and beyond. *Optica* **8**, 668–673 (2021).
12. Chen, Y. *et al.* Multiphoton resonance meets tunneling ionization: High-efficient photoexcitation in strong-field-dressed ions. *Phys. Rev. Lett.* **133**, 113201 (2024).
13. Yuen, C. & Lin, C. Probing vibronic coherence in charge migration in molecules using strong-field sequential double ionization. *Phys. Rev. A* **109**, L011101 (2024).
14. Yuen, C.-H. & Lin, C.-D. Coherence from multiorbital tunneling ionization of molecules. *Phys. Rev. A* **108**, 023123 (2023).
15. Richter, M. *et al.* Rotational quantum beat lasing without inversion. *Optica* **7**, 586–592 (2020).
16. Gao, J. *et al.* Controlling the polarization of nitrogen ion lasing. *The J. Phys. Chem. Lett.* **15**, 3805–3811 (2024).
17. Xie, H. *et al.* Role of rotational coherence in femtosecond-pulse-driven nitrogen ion lasing. *Phys. Rev. Res.* **2**, 023329 (2020).
18. Gao, J. *et al.* Structured air lasing of N₂⁺. *Commun. Phys.* **6**, 97 (2023).
19. Hu, Y. *et al.* Generation of vortex N₂⁺ lasing. *Optica* **10**, 682–687 (2023).
20. Kleine, C. *et al.* Electronic state population dynamics upon ultrafast strong field ionization and fragmentation of molecular nitrogen. *Phys. Rev. Lett.* **129**, 123002 (2022).
21. Mei, H. *et al.* Amplification of light pulses with orbital angular momentum (oam) in nitrogen ions lasing. *Opt. Express* **31**, 31912–31921 (2023).

22. Shen, B. *et al.* High-gain, high-order vortex air lasing generated by plasma amplification. *Laser & Photonics Rev.* 2401276 (2024).
23. Lu, X. *et al.* Cascaded amplification of air lasing. *Sci. Adv.* **11**, eady7458 (2025).
24. Cao, J., Fu, Y., Wang, T., Dai, Z. & Xu, H. Composite vortex air laser. *Commun. Phys.* **8**, 72 (2025).
25. Danylo, R. *et al.* Measurement of optical amplification and population dynamics using ultrafast xuv spectroscopy of N_2^+ . *Opt. Lett.* **50**, 6205–6208 (2025).
26. Liu, Z. *et al.* Extremely nonlinear raman interaction of an ultrashort nitrogen ion laser with an impulsively excited molecular wave packet. *Phys. Rev. A* **101**, 043404 (2020).
27. Zhang, N. *et al.* Electronic-resonance-enhanced coherent raman spectroscopy with a single femtosecond laser beam. *Laser & Photonics Rev.* **17**, 2300020 (2023).
28. Lu, X. *et al.* Single-shot single-beam coherent raman scattering thermometry based on optically induced air lasing. *Light. Sci. & Appl.* **13**, 315 (2024).
29. Zhang, N. *et al.* Detection of atmospheric carbon dioxide with air-lasing-based coherent raman spectroscopy. *Opt. Express* **33**, 23873–23882 (2025).
30. Lei, H. *et al.* Ultraviolet supercontinuum generation driven by ionic coherence in a strong laser field. *Nat. Commun.* **13**, 4080 (2022).
31. Gao, J. *et al.* Controlling rotational air lasing lineshape by carrier-envelope offset phase. *Nat. Commun.* **16**, 9654 (2025).
32. Gao, J. *et al.* Broadband carrier-envelope phase-controlled stimulated ultraviolet emission from carbon dioxide ions. *Phys. Rev. Lett.* **135**, 223802 (2025).
33. Ni, J. *et al.* Identification of the physical mechanism of generation of coherent N_2^+ emissions in air by femtosecond laser excitation. *Opt. Express* **21**, 8746–8752 (2013).
34. Xu, B. *et al.* Free-space N_2^+ lasers generated in strong laser fields: the role of molecular vibration. *Opt. Express* **26**, 13331–13339 (2018).
35. Luo, Q., Liu, W.-w. & Chin, S. Lasing action in air induced by ultra-fast laser filamentation. *Appl. Phys. B* **76**, 337–340 (2003).
36. Corkum, P., Ho, P., Alfano, R. & Manassah, J. Generation of infrared supercontinuum covering 3–14 μ m in dielectrics and semiconductors. *Opt. Lett.* **10**, 624–626 (1985).

37. Perry, M. D., Ditmire, T. & Stuart, B. Self-phase modulation in chirped-pulse amplification. *Opt. Lett.* **19**, 2149–2151 (1994).
38. Chu, W. *et al.* A self-induced white light seeding laser in a femtosecond laser filament. *Laser Phys. Lett.* **11**, 015301 (2013).
39. Chen, J. *et al.* Electronic-coherence-mediated molecular nitrogen-ion lasing in a strong laser field. *Phys. Rev. A* **100**, 031402 (2019).
40. Britton, M. *et al.* Short-and long-term gain dynamics in N_2^+ air lasing. *Phys. Rev. A* **100**, 013406 (2019).
41. Beresna, M., Kazansky, P. G., Svirko, Y., Barkauskas, M. & Danielius, R. High average power second harmonic generation in air. *Appl. Phys. Lett.* **95**, 121502 (2009).
42. Liu, Y., Brelet, Y., Point, G., Houard, A. & Mysyrowicz, A. Self-seeded lasing in ionized air pumped by 800 nm femtosecond laser pulses. *Opt. Express* **21**, 22791–22798 (2013).
43. Rubinsztein-Dunlop, H. *et al.* Roadmap on structured light. *J. Opt.* **19**, 013001 (2016).
44. Forbes, A., De Oliveira, M. & Dennis, M. R. Structured light. *Nat. Photonics* **15**, 253–262 (2021).
45. Cristiani, I. *et al.* Roadmap on multimode photonics. *J. Opt.* **24**, 083001 (2022).
46. Shen, Y. *et al.* Roadmap on spatiotemporal light fields. *J. Opt.* **25**, 093001 (2023).
47. Fang, Y., Lyu, Z. & Liu, Y. Ultrafast physics with structured light. *Nat. Rev. Phys.* 1–15 (2025).
48. Zhan, Q. Cylindrical vector beams: from mathematical concepts to applications. *Adv. Opt. Photonics* **1**, 1–57 (2009).
49. Dorn, R., Quabis, S. & Leuchs, G. Sharper focus for a radially polarized light beam. *Phys. Rev. Lett.* **91**, 233901 (2003).
50. Machavariani, G., Lumer, Y., Moshe, I., Meir, A. & Jackel, S. Efficient extracavity generation of radially and azimuthally polarized beams. *Opt. Lett.* **32**, 1468–1470 (2007).
51. Ramachandran, S., Kristensen, P. & Yan, M. F. Generation and propagation of radially polarized beams in optical fibers. *Opt. Lett.* **34**, 2525–2527 (2009).
52. Bethune, D. Optical second-harmonic generation in atomic vapors with focused beams. *Phys. Rev. A* **23**, 3139 (1981).

53. Schimpf, D. N., Putnam, W. P., Grogan, M. D., Ramachandran, S. & Kärtner, F. X. Radially polarized bessel-gauss beams: decentered gaussian beam analysis and experimental verification. *Opt. Express* **21**, 18469–18483 (2013).
54. Vyas, S., Kozawa, Y. & Sato, S. Generation of radially polarized bessel–gaussian beams from c-cut Nd:YVO₄ laser. *Opt. Lett.* **39**, 1101–1104 (2014).
55. Xie, H. *et al.* Anisotropic coherence induced nonuniform amplification in N₂⁺. *Sci. China Physics, Mech. & Astron.* **67**, 124204 (2024).
56. Gariepy, G. *et al.* Creating high-harmonic beams with controlled orbital angular momentum. *Phys. Rev. Lett.* **113**, 153901 (2014).
57. Hancock, S., Zahedpour, S. & Milchberg, H. Second-harmonic generation of spatiotemporal optical vortices and conservation of orbital angular momentum. *Optica* **8**, 594–597 (2021).
58. Tokizane, Y., Oka, K. & Morita, R. Supercontinuum optical vortex pulse generation without spatial or topological-charge dispersion. *Opt. Express* **17**, 14517–14525 (2009).
59. Xu, L. *et al.* Powerful supercontinuum vortices generated by femtosecond vortex beams with thin plates. *Photonics Res.* **10**, 802–809 (2022).
60. Bree, C., Demircan, A. & Steinmeyer, G. Method for computing the nonlinear refractive index via keldysh theory. *IEEE J. Quantum Electron.* **46**, 433–437 (2010).
61. Wang, T.-J. *et al.* Forward lasing action at multiple wavelengths seeded by white light from a femtosecond laser filament in air. *Phys. Rev. A* **88**, 053429 (2013).
62. Liu, Y. *et al.* Unexpected sensitivity of nitrogen ions superradiant emission on pump laser wavelength and duration. *Phys. Rev. Lett.* **119**, 203205 (2017).
63. Tsai, M.-S. *et al.* Nonlinear compression toward high-energy single-cycle pulses by cascaded focus and compression. *Sci. Adv.* **8**, eabo1945 (2022).
64. Redding, B., Choma, M. A. & Cao, H. Spatial coherence of random laser emission. *Opt. Lett.* **36**, 3404–3406 (2011).
65. Tommasini, R., Insam, S. & Fill, E. Coherence properties of an amplified spontaneous emission laser: experiments on a 10 hz vacuum–ultraviolet H₂-laser. *Opt. Commun.* **180**, 277–283 (2000).

66. Bachelard, R. *et al.* Wavefront analysis of nonlinear self-amplified spontaneous-emission free-electron laser harmonics in the single-shot regime. *Phys. Rev. Lett.* **106**, 234801 (2011).
67. Ahn, N. *et al.* Electrically driven amplified spontaneous emission from colloidal quantum dots. *Nature* **617**, 79–85 (2023).
68. Ma, X. *et al.* Vortex random fiber laser with controllable orbital angular momentum mode. *Photonics Res.* **9**, 266–271 (2021).
69. Li, H. *et al.* Monolithically integrated photonic crystal surface emitters on silicon with a vortex beam by using bound states in the continuum. *Opt. Lett.* **48**, 1702–1705 (2023).
70. Gold, D. *et al.* Spatial coherence of light in collective spontaneous emission. *PRX Quantum* **3**, 010338 (2022).
71. Tong, X.-M., Zhao, Z. & Lin, C.-D. Theory of molecular tunneling ionization. *Phys. Rev. A* **66**, 033402 (2002).
72. Pavičić, D., Lee, K. F., Rayner, D. M., Corkum, P. B. & Villeneuve, D. M. Direct measurement of the angular dependence of ionization for N₂, O₂ and CO₂ in intense laser fields. *Phys. Rev. Lett.* **98**, 243001 (2007).
73. Zhang, H. *et al.* Rotational coherence encoded in an “air-laser” spectrum of nitrogen molecular ions in an intense laser field. *Phys. Rev. X* **3**, 041009 (2013).
74. Xu, H., Lötstedt, E., Ando, T., Iwasaki, A. & Yamanouchi, K. Alignment-dependent population inversion in N₂⁺ in intense few-cycle laser fields. *Phys. Rev. A* **96**, 041401 (2017).
75. Siegman, A. E. *Lasers* (University science books, 1986).
76. Li, Y., Lewellen, J., Huang, Z., Sajaev, V. & Milton, S. V. Time-resolved phase measurement of a self-amplified free-electron laser. *Phys. Rev. Lett.* **89**, 234801 (2002).
77. Kerttula, J. *et al.* Tapered fiber amplifier with high gain and output power. *Laser Phys.* **22**, 1734–1738 (2012).
78. Lei, M., Wu, C., Zhang, A., Gong, Q. & Jiang, H. Population inversion in the rotational levels of the superradiant N₂⁺ pumped by femtosecond laser pulses. *Opt. Express* **25**, 4535–4541 (2017).
79. Miao, Z. *et al.* Optical amplification from high vibrational states of ionized nitrogen molecules generated by 800-nm femtosecond laser pulses. *Opt. Express* **29**, 2279–2287 (2021).

80. Richards, B. & Wolf, E. Electromagnetic diffraction in optical systems, ii. structure of the image field in an aplanatic system. *Proc. Royal Soc. London. Ser. A. Math. Phys. Sci.* **253**, 358–379 (1959).

Author contributions

J. G., H. J. and Yunquan L. conceived the study. J. G. performed the experiments with assistance from Y. W. and H. M.. J. G. and H. J. built the cylindrical symmetric anisotropic gain model. J. G. extended the Richard-Wolf vectorial diffraction method to the cylindrical lens case. J. G. performed the simulations. J. G., Yi L., C. W., H. J., M. H., and Yunquan L. analyzed and interpreted the data. C. W. and Yunquan L. provided elements of the experimental setup. J. G. and J. D. designed all schematics. M. H. and J. G. drafted the paper with the input from all authors.

Acknowledgments

This work was supported by the National Key R&D Program (No. 2022YFA1604301) and the Natural Science Foundation of China (No. 12334013, No. 92250306, No. 12595343, and No. 12404393).

Competing interests

The authors declare no competing interests